Aircraft Icing: In-cloud Measurements and Explicit Prediction of Supercooled Large Droplets in Icing Clouds of Eastern China using Multi-moment Microphysics Schemes

Liping Luo[1,2,3], Hongyang Wang[1], Ming Xue[4], Xi Chen[5], Jing Sun[6] and Rong Zhang[6]

[1]*College of Civil Aviation, Nanjing University of Aeronautics and Astronautics, Nanjing, China, 211106*

[2]*China Meteorological Administration Hydro-Meteorology Key Laboratory, Beijing, China. 100081*

[3]*Shanghai Typhoon Institute, China Meteorological Administration, Shanghai, China, 200030*

[4]*Center for Analysis and Prediction of Storms and School of Meteorology, University of Oklahoma, Norman, Oklahoma 73072, USA*

[5]*State Key Laboratory of Air Traffic Management System, Nanjing 210007, China*

[6]*China Meteorological Administration Weather Modification Centre, Beijing, 100081, China*

June 2026
Submitted to Geophysical Research Letters

Corresponding author:

Liping Luo (lpingluo@nuaa.edu.cn)

College of Civil Aviation, Nanjing University of Aeronautics and Astronautics, Nanjing, China, 211106

Key Points:

- In-situ aircraft observations reveal that abundant supercooled large liquid water droplets are key to rapid icing.
- Diagnostic cloud droplet shape parameter (α_c) substantially increases predicted supercooled LWC, better matching observations.
- Aircraft icing rate and intensity prediction are significantly enhanced by increased LWC from the use of diagnostic α_c.

Abstract

The characteristics of supercooled liquid water (SLW) within icing clouds over eastern China are investigated using in-situ aircraft observations and numerical simulations. SLW content increases from 0 to –4°C, but decreases sharply below –4°C. Abundant supercooled large droplets (SLD) were observed, with the effective diameter reaching 175 μm and number concentration (N_t) exceeding 19 cm^{-3}. An aircraft icing rate and intensity forecast algorithm is proposed by incorporating flight conditions and SLW spectral characteristics, together with a new diagnostic relation between cloud droplet shape parameter and N_t implemented into the three-moment NSSL scheme. Sensitivity simulations indicate that the improved scheme can reproduce well the temperature-dependent variation of SLW content, and significantly enhance forecasted rate of icing, intensity, and icing cloud layer depth.

Plain Language Summary

Aircraft icing is a common threat to flight safety. This study analyzes the characteristics of supercooled liquid water (SLW) within clouds of a severe icing event over Anqing, Anhui Province of eastern China using in-cloud aircraft observations. Observations show SLW content increases as temperature decreases from 0 °C to –4 °C, but decreases sharply below –4 °C due to conversion of water vapor into ice crystals. Specifically, abundant supercooled large droplets were observed, with maximum diameter reaching 175 μm. A forecasting algorithm for icing rate and intensity that considers aircraft flight speed, SLW content, and droplet size is proposed. We also design a diagnostic method for the shape parameter of cloud droplet spectrum, and couple it with the three-moment NSSL microphysics scheme. Numerical experiments show that the new scheme better reproduces the temperature-dependent variation of SLW, and significantly improves the forecasting skill of icing rate and intensity. In summary, diagnosing the shape parameter of the cloud droplet spectrum is critical for improving the accuracy of SLW and aircraft icing intensity forecasts.

1. Introduction

Aircraft icing refers to the phenomenon that ice accumulates on aircraft surfaces through the freezing of supercooled liquid water (SLW) or water vapor deposition. In particular, supercooled large droplets (SLD) (Cober & Isaac, 2012) can substantially increase the rate and intensity of icing (Cao et al., 2018), and severely degrade aircraft maneuverability and stability. Therefore, comprehensive knowledge of icing cloud microphysics and accurate prediction of icing occurrence and intensity are important for flight safety (Bernstein et al., 2019).

Aircraft in-situ observation is one of the most effective approaches to investigate cloud microphysical properties. Extensive research flights have been conducted in North America and Europe to characterize aircraft icing environments (e.g., Isaac et al., 1999, 2001; Cober & Isaac, 2001, 2012; Bernstein et al., 2021). For example, between 1995 and 2000, the Environment Canada (EC) and the National Aeronautics and Space Administration (NASA) Glenn Icing Technology Branch conducted six field projects, obtaining detailed observations of aircraft icing environments that included SLD (e.g., Cober et al., 2001; Isaac et al., 2001). Cober and Isaac (2012) further analyzed the flight observations of aircraft icing environments that included SLD greater than 100 μm in diameter. They segregated the SLD observations into four subsets based on the maximum drop size and median volume diameter (MVD), and developed envelopes of maximum LWC for each subset as a function of horizontal extent and temperature. More recently, Lucke et al. (2025) compared the microphysical properties of SLD between two flight campaigns performed in the Great Lakes and over France. They found that SLD conditions during the North American campaign mainly occurred in thick stratus clouds, with smaller MVDs than those during the European campaign. Such differences further demonstrate that cloud type, in-cloud temperature, vertical velocity, and microphysical properties vary significantly for different regions.

Aircraft icing forecasting methods can be mainly categorized into empirical diagnostics, statistical icing potential forecasting, and explicit cloud-resolving numerical prediction. Currently, operational icing forecasting is dominated by icing potential forecast approaches. Relevant verifications indicate that such methods can only predict the occurrence probability and intensity of icing, and suffer from high false alarm rates (Mao et al., 2023; Zhou et al., 2023). Cloud-resolving numerical models coupled with multi-moment microphysics parameterization (MP) schemes are in principle capable of explicit prediction of the three-dimensional particle size distribution (PSD) of supercooled water. For instance, Thompson et al. (2017) compared the LWC, MVD and number concentration of supercooled liquid water predicted by the operational High-Resolution Rapid Refresh (HRRR) model using partially two-moment Thompson microphysics scheme, with decades of in-situ aircraft observations collected by the United States Federal Aviation Administration. The results show that HRRR model can reasonably reproduce the droplet size distribution features of supercooled liquid water. Nevertheless, recent studies have revealed that substantial uncertainties remain in the representation of various microphysical processes and hydrometeor PSDs within MP schemes (e.g., Morrison et al., 2020; Yuan et al. 2025; Luo et al., 2026). Specifically, Jensen et al. (2023) compared HRRR

simulations with observations from the ICICLE campaign and found that the Thompson-Eidhammer scheme significantly underestimates the frequency of SLD. Current explicit predictions of supercooled cloud droplets for aircraft icing over China still contain notable biases, partly attributable to observational constrains. Operational numerical weather prediction and modeling research commonly use bulk microphysics schemes. Such schemes generally classify hydrometeors into multiple categories *x*, with $x \in [c, r, i, s, g, h]$ referring to cloud water, rainwater, ice crystals, snow, graupel and hail, respectively, and assume their PSDs conform to the Gamma distribution defined as:

$$N_x(D) = N_{0x} D^{\alpha_x} \exp(-\lambda_x D), \quad (1)$$

where $N_x(D)$ represents the total number concentration of category *x* with diameter D per unit volume, N_{0x}, α_x and λ_x denote the intercept, shape, and slope parameters of the PSD, respectively. Widely used multi-moment schemes, such as the NSSL (Mansell et al., 2010) and Morrison (Morrison et al., 2009) schemes, predict the mass mixing ratio and number concentration of cloud water (Q_c and Nt_c), from which N_{0c} and λ_c are derived, while α_c is held constant. However, studies have noted that fixed α_c cannot properly capture the tail of the PSD (Zhang et al., 2023; Luo et al., 2018). Zhang et al. (2023) developed a triple-parameter condensation scheme with α_c diagnosed, and elucidated the importance of α_c for cloud droplets PSD. The diagnosis of α_c for supercooled cloud droplets, along with its influence on aircraft icing prediction, warrants further investigation.

The primary objectives of this study are twofold: (1) to characterize the icing environment and the PSDs of SLW and SLD through analysis of in-situ aircraft icing observations in a severe icing event over eastern China; and (2) to investigate the explicit forecasting performance of multi-moment MP schemes for SLW against aircraft observations, and develop α_c diagnostic algorithm to improve SLW and icing intensity prediction**.**

2. Methodology and Experimental Design

2.1. In-cloud Measurements

On March 9 2016, the Weather Modification Center of China Meteorological Administration conducted an airborne in-situ icing detection experiment using an MA60 aircraft over Anqing, Anhui Province (Figs. 1a, 1b). During the first flight of the day, aircraft icing was observed from 0110 to 0132 UTC at approximately 3000 m with an ambient temperature of –5 °C. The observed aircraft icing was of rimed ice, with a thickness of 2-4 cm. The icing event occurred at the top of stratocumulus clouds following the end of convective precipitation under a cold front, and the icing altitude corresponded to the base of a frontal inversion layer. A detailed description of the synoptic conditions associated with this event is provided by Sun et al. (2019).

During the experiment, the MA60 was equipped with multiple sensors, including a hot-wire LWC meter, an Airborne Integrated Meteorological Measurement System (AIMMS-20), a Backscatter Cloud Probe (BCP), and a Cloud Imaging Probe (CIP). Among them, the LWC meter operates via constant-temperature hot-wire compensation. The AIMMS-20 observes environmental temperature, relative humidity, and pressure. The BCP probe covers a cloud droplet size range of 5–75 μm, which can also retrieve

the cloud droplet Nt and LWC. The CIP has a measurable range of 25–1550 μm, mainly detecting large droplets.

Besides, we developed a density-based screening method to filter out ice particles from the measurements. The bulk density (ρ_{bulk}) can be estimated using the LWC, Nt, and MVD. Assuming particles are spherical, ρ_{bulk} can be calculated as:

$$\rho_{bulk} = \frac{LWC}{Nt \times \frac{\pi}{6} \times MVD^3} \quad (2)$$

Specifically, particles with ρ_{bulk} lower than 0.5 g cm^{-3} were identified as ice, and excluded from analysis. Besides, the Cloud Particle Image Processor (CPIP) was used to verify both the results, which further confirmed the effectiveness of the density-based screening method. The excluded particles indeed exhibited typical morphological features of ice particles (Fig. S7), showing larger and darker spots relative to liquid droplets.

2.2. Quantities for Aircraft Icing

2.2.1 Aircraft Icing Rate based on Multi-moment MP Schemes

Aircraft icing rate ($Rate$) quantifies ice accretion rate on airframes. It is a vital reference for pilots to evaluate icing severity and avoid from icing zones. Previous studies have indicated that the icing rate is positively correlated with flight speed, supercooled LWC, and collection efficiency (Guardone et al., 2026). To enhance the prediction skill of icing rate using multi-moment schemes, this study further optimizes the icing rate. Initially established by Lewis et al. (1947), it has been widely adopted in studies on aircraft icing and wire icing (Thompson et al., 2017).

Based on the typical flight speeds of modern commercial aircraft during descent and cloud penetration, this study assumes a standard 3-inch-diameter cylinder (approximately 7.62 cm) moving at a speed of 329 miles per hour (approximately 147.22 m s^{-1}). This cylinder serves as a proxy for aircraft leading-edge icing severity (Lewis et al., 1947). $Rate$ based on the simulations using multi-moment schemes is defined as:

$$Rate = \frac{\alpha_1 \, LWC_{SLW} \, v \, \mathrm{A}}{6\rho_{\mathrm{i}}}, \quad (3)$$

where α_1 is the collision efficiency, LWC_{SLW} denotes the total supercooled LWC of cloud water and rainwater (g m^{-3}), A indicates the cross-sectional area of the standard cylinder (m^2), v denotes flight velocity (m s^{-1}), and ρ_i represents ice density, fixed at 0.917 g cm^{-3}. The specific formula for α_1 follows Thompson et al. (2017):

$$\alpha_1 = \mathrm{X} - 0.028 - \mathrm{Z}(\mathrm{Y} - 0.0454) \quad (4)$$

$$\mathrm{X} = 1.066\mathrm{K}^{-0.00616}\exp(-1.103\mathrm{K}^{-0.688}) \quad (5)$$

$$\mathrm{Y} = 3.641\mathrm{K}^{-0.498}\exp(-1.497\mathrm{K}^{-0.694}) \quad (6)$$

$$\mathrm{Z} = 0.00637(\phi - 100)^{0.381} \quad (7)$$

$$\mathrm{K} = \frac{\rho_w MVD_{SCW}{}^2 v}{9\mu_{\mathrm{a}}\mathrm{D}} \quad (8)$$

$$\phi = \frac{\mathrm{Re}^2}{\mathrm{K}} \quad (9)$$

$$\mathrm{Re} = \frac{\rho_a MVD_{SCW} \upsilon}{\mu_a} \tag{10}$$

$$\mu_a = \frac{0.001779}{1+0.03368T_a+0.0002210{T_a}^{2^2}} \tag{11}$$

$$LWC_{SLW} = (q_c + q_r) \times \rho_a \quad when \quad T < 0℃. \tag{12}$$

Herein, K is the Stokes number, characterizing the deviation degree of droplets moving along with airflow and acts as a key factor determining the collection coefficient. Re is the droplet Reynolds number, affecting the drag coefficient and trajectory of droplets. ϕ is the Langmuir parameter, describing the curvature characteristics of droplet trajectory. μ_a, T_a and ρ_a are air dynamic viscosity coefficient, temperature (°C), and density, respectively. In Eqs. (8) and (10), MVD_{SLW} (μm) represents the mass-weighted *MVD* of supercooled cloud water and rain water predicted by multi-moment schemes,

$$MVD_{SLW} = \frac{MVD_c \times q_c + MVD_r \times q_r}{q_c + q_r} \quad when \quad T < 0℃, \tag{13}$$

$$MVD_x = \frac{\int_0^\infty D \times N_x(D) dD}{\int_0^\infty N_x(D) dD}, \tag{14}$$

In this study, the three-moment NSSL MP scheme (Mansell et al., 2010) is adopted, within which α_r can be diagnosed from the radar reflectivity of rain (Eqs. 15–16), while α_c is fixed as zero.

$$Z_r = \frac{G(\alpha_r)}{c_r^2} \frac{(pq_r)^2}{N_{Tr}} \tag{15}$$

$$G(\alpha_r) = \frac{(6+\alpha_r)(5+\alpha_r)(4+\alpha_r)}{(3+\alpha_r)(2+\alpha_r)(1+\alpha_r)} \tag{16}$$

Furthermore, long-term observations indicate that α_c generally ranges between 0 and 12 over the East Asian monsoon region (Yin et al., 2011). Therefore, following Thompson (2008), this study develops a diagnostic method for α_c based on total cloud droplet number concentration (N_{Tc}) given in Eq. (17),

$$\alpha_c = \min(12, \frac{10^7}{N_{Tc}} + 2) \tag{17}$$

The diagnostic method for α_c is implemented into the NSSL three-moment scheme, and its impacts on aircraft icing prediction are evaluated. To better represent icing intensity, we convert the icing rate to mm min^{-1}. The corresponding thresholds for each icing intensity level (trace, light, moderate, and severe) are defined in Table S2.

2.2.2 Aircraft Icing Layer Depth

Based on the aforementioned formulas for $Rate$, we propose a new parameter, i.e., aircraft icing layer depth ($Depth$, in meters), defined as the cumulative depth of model layer *k* with the icing rate $Rate_k$ exceeds 0.01 mm min^{-1}, by

$$Depth = \sum_0^{nz} \Delta Depth_k \quad when \quad Rate_k > 0.01 \text{ mm min}^{-1}. \tag{18}$$

2.3. Configuration of the WRF Simulations

Simulations of the aircraft icing event are conducted using the Weather Research and Forecasting (WRF) model version 4.7.0 (Skamarock et al., 2019). The ERA5 reanalysis datasets (0.25°×0.25° resolution, 1-h intervals, Hersbach et al., 2020) are used as the

initial and boundary conditions for the simulations. Two one-way nested domains with horizontal grid spacings of 9 km and 3 km are employed (Fig.1c). Both domains utilize 49 hybrid vertical coordinate levels extending from the surface to 10 hPa, using a terrain-following coordinate near the ground and transitioning to isobaric levels above approximately 12 km (Beck et al., 2020; Skamarock et al., 2019). The simulations were initialized at 1800 UTC on March 8 and integrated until 0000 UTC on March 10, encompassing most of the lifecycle of the frontal system and the entire aircraft flight segments. The radiation, planetary boundary layer, and surface physics schemes follow those of Luo et al. (2026).

To investigate the impacts of diagnostic α_c on the simulated PSDs of SLW and the prediction of icing intensity, three sensitivity experiments are conducted (see Table S1), namely, experiments NSSL_2mom and NSSL_3mom using the NSSL two-moment and three-moment schemes, with a fixed α_c of 0; and NSSL_3mom_diag using the three-moment scheme with a diagnostic α_c calculated by Eq. (17).

3. Results

3.1 Characteristics of SLW and SLD for Aircraft Icing

AIMMS observations showed that the aircraft climbed to 3200 m at 0100 UTC, where the ambient temperature dropped below 0 °C and subsequently remained between –2 °C and –8 °C at altitudes of 3000–4600 m. Throughout the flight, the ambient relative humidity remained high (>90%), indicating conditions favorable for supercooled water and aircraft icing (e.g., Bernstein et al., 2005; Cober & Isaac, 2012). BCP observations revealed that between 0120 and 0150 UTC, N_{tc} and LWC of SLW increased significantly, reaching 62 cm^{-3} and 0.29 g m^{-3}, respectively (Figs. 2a1, a2, a4). The effective diameter (*ED*) of SLW was 20~25 μm (Fig. 2a3). During this period, CIP observations showed abundant SLD, with *ED* and N_{tc} exceeding 175 μm and 19 cm^{-3}, respectively, and LWC of ~0.061 g m^{-3} (Figs. 2b1–b4). This was also consistent with the records of onboard personnel, who noted that rapid icing beginning at 0136 UTC with ambient temperature of approximately –5 °C (Sun et al., 2019). Between 0300 and 0330 UTC, both BCP and CIP again detected SLD, with CIP showing a further increase in *ED* to 200 μm and N_{tc} of ~1.57 cm^{-3} (Figs. 2b1–b4). Ultimately, the aircraft icing thickness reached approximately 2-4 cm during this event.

3.2 Validation of Explicit Prediction of SLW

To quantitatively assess the prediction skill of different simulations for SLW, the simulated temperature-dependent characteristics of LWC and PSDs of SLW are compared with in-situ aircraft observations (Fig. 3). Those of LWC over the entire inner domain are also examined (Fig. S3). The observations showed that LWC occurred predominantly at temperatures above –6 °C (accounting for 94.7% of the occurrences). The 50th percentile of LWC shows little variation with temperature, while the 90th, 95th, and 99th percentiles of LWC varied significantly with temperature (Fig. 3a3). Between 0 °C and –4 °C, these percentiles increased with decreasing temperature, reaching their peak values near –4 °C of 0.1399, 0.2137, and 0.2901 g m^{-3}, respectively (Fig. 3a3, Table S3). This was likely associated with weak updrafts within stratiform

clouds, which transport more water vapor above the freezing level, that generate increasing amounts of supercooled water as the temperature drops from 0°C to –4°C (Thompson et al., 2017). Below –4 °C, LWC decreased significantly with decreasing temperature. The supercooled water reduction could result from both intensified Wegener-Bergeron-Findeisen (BWF) process at lower temperature and entrainment-driven mixing near cloud top (Cober & Isaac, 2012; Ricaud et al., 2020).

We note that with α_c fixed at 0, simulations NSSL_2mom and NSSL_3mom yield similar Q_c, Nt_c, and PSDs (Figs. S1, S2, S4). Thus, it appears that the prediction of additional radar reflectivity for hail and rain in NSSL_3mom compared to NSSL_2mom has minimal impacts on the prediction of SLW. Thus, we focus on comparing the differences between the NSSL_3mom and NSSL_3mom_diag simulations. To exclude the influence of convective clouds, we applied a reflectivity-based filter (mdbz < 30 dBZ) to isolate stratiform regions. Results show that extensive high-LWC values are distributed within the 0 °C to –4 °C layer in both simulations (Figs.3a1-a2). The maximum 90th percentile of LWC from NSSL_3mom and NSSL_3mom_diag over southwest Anhui region are significantly higher than the observations (NSSL_3mom: 0.2952 g m^{-3}, NSSL_3mom_diag: 0.309 g m^{-3}, observation: 0.1399 g m^{-3}) (Figs. 3a1, a2, Table S3). On the other hand, within the –4 °C to –8 °C layer, the simulated LWC decreasing rates are substantially stronger than those observed (Figs.3a1-a3). This discrepancy may stem partly from flight-sampling strategy (Thompson et al., 2017), but may also attribute to the overestimation of BWF process within the NSSL scheme (Nam et al., 2024; Zhang et al., 2025). Notably, the maximum 99.9th percentile of LWC from NSSL_3mom_diag is ~9% higher than that from NSSL_3mom and closer to the observations, demonstrating the improvement in explicit prediction of SLW achieved by the diagnostic α_c (NSSL_3mom: 0.4083 g m^{-3}, NSSL_3mom_diag: 0.4467 g m^{-3}, observation: 0.3140 g m^{-3}, Table S3).

For the entire inner domain, the 50th percentile of LWC from different simulations remains largely unchanged with temperature, whereas the 90th, 95th, and 99th percentiles decrease slowly as temperature fell from 0°C to –6 °C, and remain nearly constant below –6 °C (Fig. S3). This may be attributed to the development of extensive cumulus clouds and even convective clouds, where stronger updrafts transport supercooled water to higher altitudes (Van Lier-Walqui et al., 2016; Zhao et al., 2025). Moreover, the 50th, 90th, 95th, and 99th percentiles of LWC from NSSL_3mom_diag are 10–17% higher than those from NSSL_3mom (Fig. S3, Table S3). This finding aligns with the comparison from the specific aircraft observation regions and further demonstrates that diagnosing the cloud droplet shape parameter improves the explicit simulation of SLW.

Figure 3b1 shows the PSDs of supercooled cloud droplets at grid points with high icing rates over the aircraft observation regions (c.f., red dashed box in Fig. 1c) from the NSSL_3mom and NSSL_3mom_diag simulations. Figure 3b2 presents the supercooled PSDs (scatters and fitted curves) observed by the BCP and CIP probes at aircraft cruising altitudes of 3000 m and 4000 m. It shows that the PSD of supercooled cloud droplets in the NSSL_3mom follows an exponential form and is broader than the observations due to the fixed α_c of zero. In contrast, the PSD of supercooled cloud

droplets in NSSL_3mom_diag follows a gamma distribution, exhibiting a narrower spectrum than in NSSL_3mom, and is much closer to the aircraft observations (Figs. 3b1–b2). The PSDs further affect the calculation of microphysical processes contributing to supercooled droplet growth, thereby influencing icing intensity forecasts.

3.3 Aircraft Icing Prediction and Impacts of Diagnosed α_c of SLW

Given that the NSSL_3mom_diag simulation successfully reproduces the observed LWC and PSD of supercooled cloud water, we further evaluate the performance of the proposed $Rate$ and $Depth$, along with the impacts of diagnosed α_c.

The predicted column-maximum $Rate$, icing intensity, and $Depth$ at 0200UTC March 9 from the simulations over the inner domain, along with their differences are investigated (Figs. 4, S5). We found that the NSSL_3mom_diag significantly enhances the predicted $Rate$ and intensity, particularly over the convective cloud regions (Figs. 4a–4e). The 50th and 90th percentiles of the difference in $Rate$ between NSSL_3mom_diag and NSSL_3mom are 0.70 mm min^{-1} and 2.05 mm min^{-1}, respectively (Fig. 4c). Statistics of icing intensity differences show a significant reduction in the proportion of trace and light icing, with trace icing frequency decreases from 31.0% to 15.2%, and light icing frequency from 52.0% to 49.0%. In contrast, the frequencies of moderate and severe icing increase significantly, from 14.2% to 27.2% and from 2.7% to 8.7%, respectively (Fig. 4f). Moreover, the predicted $Depth$ in NSSL_3mom_diag is substantially larger than that in NSSL_3mom, with the 50th and 90th percentile differences reaching 314.34 m and 1168.34 m, respectively (Figs. 4g-i). We also note that differences in $Rate$, intensity, and $Depth$ between NSSL_2mom and NSSL_3mom are negligible (Fig. S5), consistent with their identical supercooled LWC and droplet size distributions (Figs. S1–S4). These results further demonstrate that the implemented diagnostic α_c significantly improves aircraft icing intensity forecasts, consistent with the earlier finding that NSSL_3mom_diag successfully reproduces high supercooled LWC and a more realistic supercooled cloud PSD. We note that the diagnostic equation is based on a single aircraft icing case, and its applicability across different climatic regions and varying environmental conditions requires further evaluations. Nevertheless, preliminary validation over Southwest China using one-year independent simulations shows encouraging prediction skill (Tables S4, S5), suggesting promising cross-regional applicability of the method.

4. Conclusions

In this study, in-situ aircraft observations of an aircraft icing event over Anhui Province, China, are analyzed to investigate the microphysical properties and supercooled droplet size distribution in the event. In addition, a new cloud-resolving model-based quantity for aircraft icing rate and intensity has been proposed, accounting for aircraft flight speed, combined PSDs of supercooled cloud water and rain, and the collection efficiency. A diagnostic method for the shape parameter of cloud droplet size distribution has been developed and coupled with the three-moment NSSL MP scheme within the WRF model.

In-situ aircraft observations revealed abundant SLW during the icing event. In particular, the aircraft encountered a large number of SLDs, with the CIP probe recording an effective diameter of 175 μm and a number concentration exceeding 19 cm^{-3}, which are likely responsible for the rapid icing. Between 0 °C and −4 °C, the 90th, 95th, and 99.9th percentiles of LWC increased with decreasing temperature. This may be driven by weak stratiform-cloud updrafts transporting water vapor above the freezing level, and latent-heat release from ice formation that amplifies vertical motion and enhances LWC. Below –4 °C, LWC decreased sharply with decreasing temperature, which may be related to intensified BWF process and entrainment-driven mixing near cloud top. Besides, sensitivity simulations using different versions of the NSSL scheme were conducted to evaluate the performance of the cloud-resolving model in predicting supercooled water and aircraft icing. Results show that the NSSL_2mom and NSSL_3mom simulations, using two- and three-moment NSSL schemes with fixed α_c, produce essentially identical SCW distributions, leading to comparable forecasts of aircraft icing rate and intensity. We found that NSSL_3mom_diag with a diagnostic α_c better reproduces the observed temperature-dependent variations of LWC than other simulations. Across the entire inner domain, the 50th, 90th, 95th, and 99th percentiles of LWC in NSSL_3mom_diag are 10–17% higher than those in NSSL_3mom, further demonstrating that diagnosing α_c promotes the growth of SCW. Moreover, compared to NSSL_3mom, NSSL_3mom_diag predicts significantly enhanced aircraft icing rate and intensity over convective cloud regions, increased frequencies of moderate and severe icing intensities, and a substantially deeper icing layer.

We believe this study represents the first effort in forecasting aircraft icing rate and intensity based on explicit supercooled water prediction using multi-moment microphysics schemes within a cloud-resolving model. We acknowledge that the conclusions drawn in this study are based on a single aircraft icing case and its corresponding simulations. Although preliminary validations based on one-year simulations over Southwest China exhibit encouraging aircraft-icing forecast skill, the applicability of these diagnostic equations to other climatic regions under varied environmental conditions remains to be verified. We hope this study would serve as a call for the community for increased in-situ aircraft icing observations and cloud-resolving model-based icing forecasting research, while paying close attention to cloud microphysical properties and aircraft aerodynamic configurations.

Acknowledgements

This work was primarily sponsored by the National Natural Science Foundation of China (42475200), and the Aviation Science Fund of China (2024M074052002). This work was also funded by Shanghai Typhoon Institute, China Meteorological Administration (TFJJ202406), Open Foundation of China Meteorological Administration Hydro-Meteorology Key Laboratory (24SWQXZ010), Nanjing Joint Institute for Atmospheric Sciences (BJG202505), and Meteorological Joint Fund Project of Guangdong Province (2024A1515510010).

Availability Statement

Computational support was provided by High Performance Computing Platform of Nanjing University of Aeronautics and Astronautics. Simulation forcing is from ERA5 (Hersbach et al., 2023; Hersbach et al., 2020). Modeling data produced by this study as well as the verification data are available on Zenodo (Wang, 2026).

Conflict of Interest Statement

The authors declare no conflicts of interest relevant to this study.

References

Beck, J., Brown, J., Dudhia, J., Gill, D., Hertneky, T., Klemp, J., Wang, W., Williams, C., Hu, M., James, E., Kenyon, J., Smirnova, T., & Kim, J.-H. (2020). An evaluation of a hybrid, terrain-following vertical coordinate in the WRF-based RAP and HRRR models. *Weather and Forecasting*, *35(3)*, 1085–1096. https://doi.org/10.1175/WAF-D-19-0146.1.

Bernstein, B. C., McDonough, F., Politovich, M. K., Brown, B. G., Ratvasky, T. P., Miller, D. R., Wolff, C. A., & Cunning, G. (2005). Current Icing Potential: Algorithm Description and Comparison with Aircraft Observations. *Journal of Applied Meteorology and Climatology*, *44(7)*, 969–986. https://doi.org/10.1175/JAM2246.1.

Bernstein, B. C., Rasmussen, R. M., McDonough, F., & Wolff, C. (2019). Keys to Differentiating between Small- and Large-Drop Icing Conditions in Continental Clouds. *Journal of Applied Meteorology and Climatology*, *58(9)*, 1931–1953. https://doi.org/10.1175/JAMC-D-18-0038.1.

Bernstein, B. C., DiVito, S., Riley, J. T., Landolt, S., Haggerty, J., Thompson, G., Adriaansen, D., Serke, D., Kessinger, C., Tessendorf, S., Wolde, M., Korolev, A., Brown, A., Nichman, L., Sims, D., & Dumont, C. (2021). The In-Cloud Icing and Large-Drop Experiment Science and Operations Plan (DOT/FAA/TC-21/29). Atlantic City International Airport, NJ: Federal Aviation Administration.

Cober, S. G., & Isaac, G. A. (2012). Characterization of Aircraft Icing Environments with Supercooled Large Drops for Application to Commercial Aircraft Certification. *Journal of Applied Meteorology and Climatology*, *51(2)*, 265–284. https://doi.org/10.1175/JAMC-D-11-022.1.

Cober, S. G., G. A. Isaac, & Strapp, J. W. (1995). Aircraft Icing Measurements in East Coast Winter Storms. *Journal of Applied Meteorology and Climatology*, *34(1)*, 88–100. https://doi.org/10.1175/1520-0450-34.1.88.

Cober, S. G., G. A. Isaac, & Strapp, J. W. (2001). Characterizations of Aircraft Icing Environments that Include Supercooled Large Drops. *Journal of Applied Meteorology*, *40(11)*, 1984–2002. https://doi.org/10.1175/1520-0450(2001)040<1984:COAIET>2.0.CO;2.

Cao, Y., Tan, W., & Wu, Z. (2018). Aircraft icing: An ongoing threat to aviation safety. *Aerospace Science and Technology*, *75*, 353–385. https://doi.org/10.1016/j.ast.2017.12.028.

Guardone, A., Bellosta, T., Donizetti, A., & Gallia, M. (2026). Aircraft icing: Modeling and simulation. *Annual Review of Fluid Mechanics*, *58*, 139–165. https://doi.org/10.1146/annurev-fluid-112723-062537.

Hersbach, H., Bell, B., Berrisford, P., Hirahara, S., Horányi, A., Muñoz-Sabater, J., Nicolas, J., Peubey, C., Radu, R., Schepers, D., Simmons, A., Soci, C., Abdalla, S., Abellan, X., Balsamo, G., Bechtold, P., Biavati, G., Bidlot, J., Bonavita, M., De Chiara, G., Dahlgren, P., Dee, D., Diamantakis, M., Dragani, R., Flemming, J., Forbes, R., Fuentes, M., Geer, A., Haimberger, L., Healy, S., Hogan, R. J., Hólm, E., Janisková, M., Keeley, S., Laloyaux, P., Lopez, P., Lupu, C., Radnoti, G., de Rosnay, P., Rozum, I., Vamborg, F., Villaume, S., & Thépaut, J.-N. (2020). The

ERA5 global reanalysis. *Quarterly Journal of the Royal Meteorological Society*, *146(730)*, 1999–2049. https://doi.org/10.1002/qj.3803.

Hersbach, H., Bell, B., Berrisford, P., Biavati, G., Horányi, A., Muñoz Sabater, J., Nicolas, J., Peubey, C., Radu, R., Rozum, I., Schepers, D., Simmons, A., Soci, C., Dee, D., Thépaut, J-N. (2023): ERA5 hourly data on single levels from 1940 to present. [Dataset]. Copernicus Climate Change Service (C3S) Climate Data Store (CDS), DOI: 10.24381/cds.adbb2d47.

Isaac, G., Cober, S., Korolev, A., Strapp, J., & Tremblay, A. (1999). Canadian Freezing Drizzle Experiment. 37th Aerospace Sciences Meeting and Exhibit, Reno, NV, U.S.A. American Institute of Aeronautics and Astronautics. https://doi.org/10.2514/6.1999-492.

Isaac, G., S. G. Cober, J. W. Strapp, A. Korolev, A. Tremblay, & D. L. Marcotte (2001). Recent Canadian Research on Aircraft In-Flight Icing. *Canadian Aeronautic and Space Journal*, *44*, 213–222.

Jensen, A. A., Thompson, G., Ikeda, K., & Tessendorf, S. A. (2023). Improving the representation of hail in the Thompson microphysics scheme. *Monthly Weather Review*, *151(9)*, 2307–2332. https://doi.org/10.1175/MWR-D-21-0319.1.

Jung, Y., Xue, M., & Zhang, G. (2010). Simulations of Polarimetric Radar Signatures of a Supercell Storm Using a Two-Moment Bulk Microphysics Scheme. *Journal of Applied Meteorology and Climatology*, *49(1)*, 146–163. https://doi.org/10.1175/2009JAMC2178.1.

Lucke, J. R., Hariri, S., Dupuy, R., Schwarz, C., Dezitter, F., Weber, M., Bretschneider, L., Kaufmann, S., Schwarzenboeck, A., Dezitter, F., & Voigt, C. (2025). Microphysical properties of supercooled large droplet conditions in North America and Europe. *Journal of Air Transportation*, *33(3)*, 1–22. https://doi.org/10.2514/1.D0469

Luo, L., Xue, M., Zhu, K., & Zhou, B. (2018). Explicit Prediction of Hail in a Long-Lasting Multicellular Convective System in Eastern China Using Multimoment Microphysics Schemes. *Journal of the Atmospheric Sciences*, *75(9)*, 3115–3137. https://doi.org/10.1175/JAS-D-17-0302.1.

Luo, L., Xue, M., Zhu, K., & Wang, Z. (2021). Diagnosing the shape parameters of the gamma particle size distributions in a two-moment microphysics scheme and improvements to explicit hail prediction. *Atmospheric Research*, *258*, 105651. https://doi.org/10.1016/j.atmosres.2021.105651.

Luo, L., Xue, M., Xu, X., Deng, L., Li, J., & Zhang, R. (2026). Case study of aircraft icing in-cloud measurements and explicit supercooled water prediction in Eastern China. *Atmospheric Research*, *334*, 108748. https://doi.org/10.1016/j.atmosres.2026.108748.

Lewis, W., Kline, D. B., & Steinmetz, C. P. (1947). A further investigation of the meteorological conditions conducive to aircraft icing (Technical Note No. TN-1424). Washington, DC: National Advisory Committee for Aeronautics.

Mansell, E. R., Ziegler, C. L., & Bruning, E. C. (2010). Simulated Electrification of a Small Thunderstorm with Two-Moment Bulk Microphysics. *Journal of the Atmospheric Sciences*, *67(1)*, 171–194. https://doi.org/10.1175/2009JAS2965.1.

Mao, X., Liu, X. H., & Yang, B. (2023). An Optimized Probabilistic Prediction Method for Aircraft Icing Potential Based on a Convection-Allowing Model. Chinese *Journal of Atmospheric Sciences*, *47(5)*, 1525–1540. https://doi.org/10.3878/j.issn.1006-9895.2207.21235.

Morrison, H., Thompson, G., & Tatarskii, V. (2009). Impact of Cloud Microphysics on the Development of Trailing Stratiform Precipitation in a Simulated Squall Line: Comparison of One- and Two-Moment Schemes. *Monthly Weather Review*, *137(3)*, 991–1007. https://doi.org/10.1175/2008MWR2556.1.

Morrison, H., van Lier-Walqui, M., Fridlind, A. M., Grabowski, W. W., Harrington, J. Y., Hoose, C., Korolev, A., Kumjian, M. R., Milbrandt, J. A., Pawlowska, H., Posselt, D. J., Prat, O. P., Reimel, K. J., Shima, S.-I., van Diedenhoven, B., & Xue, L. (2020). Confronting the challenge of modeling cloud and precipitation microphysics. *Journal of Advances in Modeling Earth Systems*, *12(8)*, e2019MS001689. https://doi.org/10.1029/2019MS001689.

Nam, J., Cho, Y., Lim, K.-S., Jun, S.-Y., Kim, J.-H., Park, S.-J., & Kim, S.-W. (2024). Evaluation of four cloud microphysical schemes simulating Arctic low-level clouds observed during the ACLOUD experiment. Asia-Pacific Journal of Atmospheric Sciences, 60(5), 727 – 740. https://doi.org/10.1007/s13143-024-00378-0.

Ricaud, P., Del Guasta, M., Bazile, E., Azouz, N., Lupi, A., Durand, P., Attié, J.-L., Veron, D., Guidard, V., & Grigioni, P. (2020). Supercooled liquid water cloud observed, analysed, and modelled at the top of the planetary boundary layer above Dome C, Antarctica. Atmospheric Chemistry and Physics, 20(7), 4167–4191. https://doi.org/10.5194/acp-20-4167-2020.

Scröder, F., Welte, D., & Hauf, T. (2000). Airborne observations of ice accretion and aircraft performance in artificial and natural supercooled ice clouds on Dornier 228- and 328 aircraft. In ICAS 2000: 22nd International Congress of the Aeronautical Sciences, Harrogate, UK.

Skamarock, W. C., Klemp, J. B., Dudhia, J., Gill, D. O., Berner, R. B., Duda, M. G., Huang, X.-Y., Wang, X., & Powers, J. G. (2019). A Description of the Advanced Research WRF Model Version 4 (NCAR Tech. Note NCAR/TN-556+STR). Boulder, CO: National Center for Atmospheric Research.

Sun, J., Cai, M., Wang, F., et al. (2019). A Case Study of Aircraft Icing Conditions in Anqing Area. *Meteorological Monthly*, *45(10)*, 1341–1351. https://doi.org/10.7519/j.issn.1000-0526.2019.10.001.

Thompson, G., Field, P. R., Rasmussen, R. M., & Hall, W. D. (2008). Explicit Forecasts of Winter Precipitation Using an Improved Bulk Microphysics Scheme. Part II: Implementation of a New Snow Parameterization. *Monthly Weather Review*, *136(12)*, 5095–5115. https://doi.org/10.1175/2008MWR2387.1.

Thompson, G., Politovich, M. K., & Rasmussen, R. M. (2017). A numerical weather model's ability to predict characteristics of aircraft icing environments. *Weather and Forecasting*, *32(1)*, 207–221. https://doi.org/10.1175/WAF-D-16-0125.1.

Van Lier-Walqui, M., Fridlind, A. M., Ackerman, A. S., Collis, S., Helmus, J., MacGorman, D. R., North, K., Kollias, P., & Posselt, D. J. (2016). On Polarimetric

Radar Signatures of Deep Convection for Model Evaluation: Columns of Specific Differential Phase Observed during MC3E. *Monthly Weather Review*, *144(2)*, 737–758. https://doi.org/10.1175/MWR-D-15-0100.1.

Wang, H., (2026). Replication Data for article: Aircraft Icing: In-cloud Measurements and Explicit Prediction of Supercooled Large Droplets using Multi-moment Microphysics Schemes in Eastern China [Dataset]. Zenodo. https://doi.org/10.5281/zenodo.20410097

Yin, J. F., Wang, D. H., & Zhai, G. Q. (2011). Long-term in situ measurements of the cloud-precipitation microphysical properties over East Asia. *Atmospheric Research*, *102(1)*, 206–217. https://doi.org/10.1016/j.atmosres.2011.07.002.

Yuan, M., Lv, A., Wang, W. J., Dong, X. B., & Ping, F. (2025). The Microphysical Properties and Processes in In-Flight Icing: A Case Study. *Atmospheric Research*, *326*, 108326. https://doi.org/10.1016/j.atmosres.2025.108326.

Zhang, J., Sun, J., Deng, W., Hu, W., & Wang, Y. (2023). The importance of the shape parameter in a bulk parameterization scheme to the evolution of the cloud droplet spectrum during condensation. *Advances in Atmospheric Sciences*, *40(1)*, 155–167. https://doi.org/10.1007/s00376-022-2065-7.

Zhang, Z., Ma, S., Cheng, W., Zhu, J., Li, P., Li, F., & Zhou, L. (2025). Evaluation of Polar-WRF microphysics schemes for simulations of lower atmospheric processes in the Svalbard region, Arctic. Atmospheric Research, 330, 108597. https://doi.org/10.1016/j.atmosres.2025.108597

Zhao, C., Zhang, Y., Zhai, H., Li, Z., Zheng, D., Peng, X., Yao, W., Du, S., & Du, Y. (2025). Bridging the polarimetric structure and lightning activity of isolated thunderstorm cells during the cloud life cycle. *Atmospheric Chemistry and Physics*, *25(20)*, 13453–13473. https://doi.org/10.5194/acp-25-13453-2025.

Zhou, X. X., Li, Y. Y., & Zhang, C. (2023). Study on the Forecasting Method and Application Scenario of Aircraft Icing. *Meteorological Monthly*, *49(4)*, 415–426. https://doi.org/10.7519/j.issn.1000-0526.2023.030702.

List of Figures

Figure 1. (a) time series of the flight altitude (m), atmospheric temperature (°C) and relative humidity (%) between 00:40 and 03:50 UTC on March 9, 2016 during the icing event; (b) three-dimensional aircraft flight path colored with air temperature; and (c) two nested WRF model domain d01, d02 at 9-km and 3-km resolutions with terrain elevation (m AMSL) in color. The red dashed rectangle in panel (c) denotes the general aircraft observation region.

Figure 2. Measurement of cloud droplet by the BCP probe including (a1) the number concentration (#/cm^3), (a2) liquid water content (LWC) (g/m^3), (a3) effective diameter (ED) (um), and (a4) cloud droplet spectrum between 00:40 and 03:50 UTC on March 9, 2016 during the icing event. Panels (b1)–(b4) show the time series of corresponding variables based on the CIP probe observations.

Figure 3. Scatterplot of temperature (°C) and LWC (mg/m^3) with the 50th, 90th, 95th, 99th, and 99.9th percentiles for each degree Celsius from (a1, a2) simulations NSSL_3mom and NSSL_3mom_diag, and (a3) aircraft in-situ observations during the icing event. The PSDs of supercooled cloud droplets at the grids with maximum icing rate from the simulations are present in panel (b1), and the particle spectrum (scatters and fitted curves) observed by the BCP and CIP probes at aircraft cruising altitudes of 3000 and 4000 m are present in panel (b2).

Figure 4. Aircraft icing rate (mm/min), intensity, and icing layer depth (m) at 0200 UTC on 9 March 2016 from simulations NSSL_3mon (a, d, g), and NSSL_3mom_diag (b, e, h), respectively. Note that the differences of the parameters between the two simulations are also shown in (c, f, i), with the 50th and 90th percentiles of the differences labeled in black on panels (c, i).

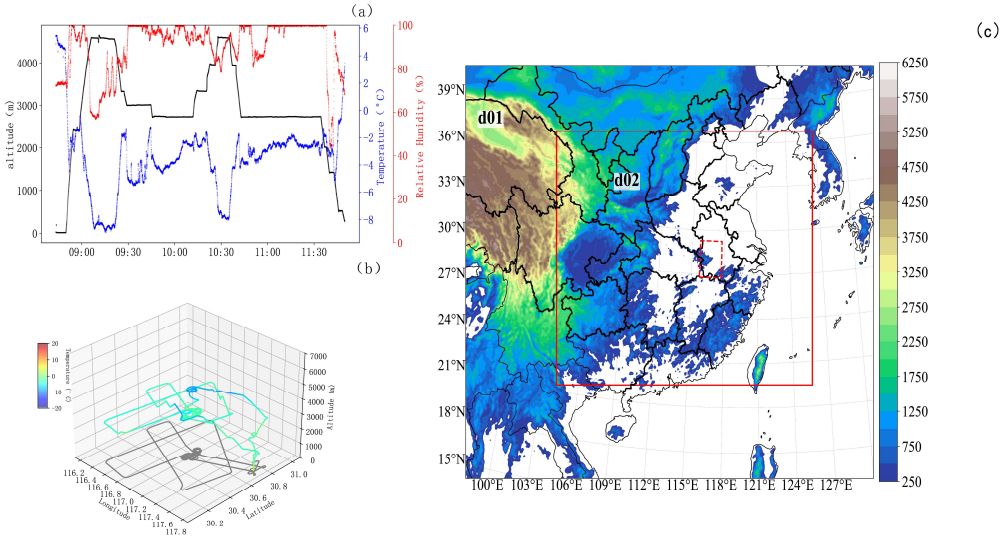


Figure 1. (a) time series of the flight altitude (m), atmospheric temperature (ºC) and relative humidity (%) between 00:40 and 03:50 UTC on March 9, 2016 during the icing event; (b) three-dimensional aircraft flight path colored with air temperature; and (c) two nested WRF model domain d01, d02 at 9-km and 3-km resolutions with terrain elevation (m AMSL) in color. The red dashed rectangle in panel (c) denotes the general aircraft observation region.

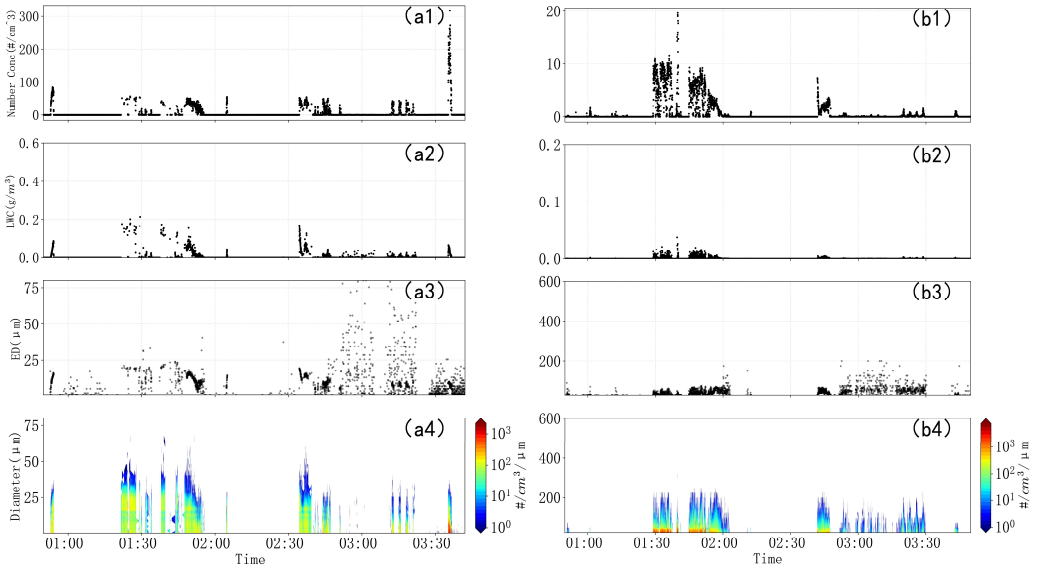
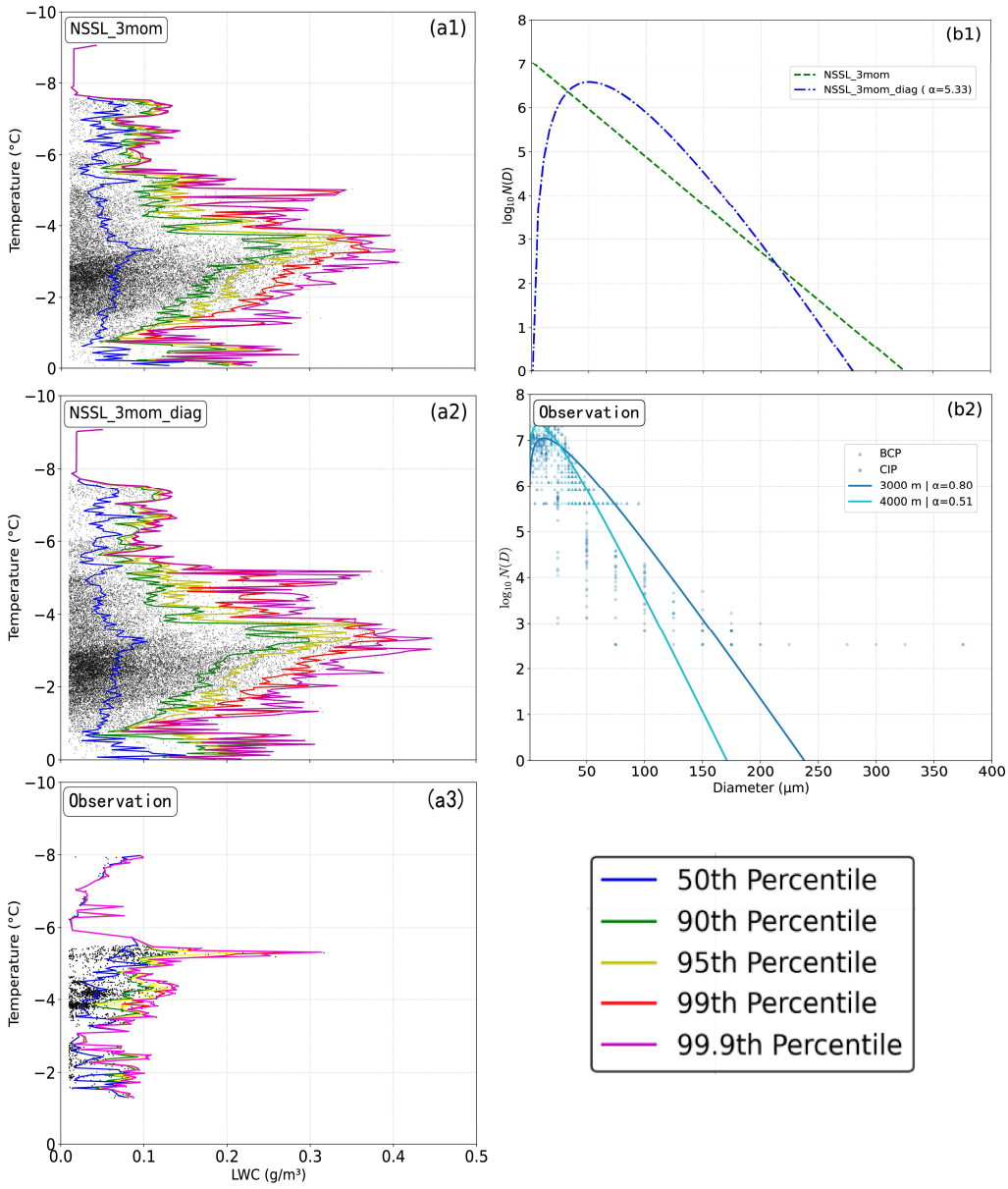


Figure 2. Measurement of cloud droplet by the BCP probe including (a1) the number concentration (#/cm³), (a2) liquid water content (LWC) (g/m³), (a3) effective diameter (ED) (um), and (a4) cloud droplet spectrum between 00:40 and 03:50 UTC on March 9, 2016 during the icing event. Panels (b1)–(b4) show the time series of corresponding variables based on the CIP probe observations.



603

604 Figure 3. Scatterplot of temperature (°C) and LWC (g/m³) with the 50th, 90th, 95th,
605 99th, and 99.9th percentiles for each degree Celsius from (a1, a2) simulations
606 NSSL_3mom and NSSL_3mom_diag, and (a3) aircraft in-situ observations during the
607 icing event. The PSDs of supercooled cloud droplets at the grids with maximum icing
608 rate from the simulations are present in panel (b1), and the particle spectrum (scatters
609 and fitted curves) observed by the BCP and CIP probes at aircraft cruising altitudes of
610 3000 and 4000 m are present in panel (b2).

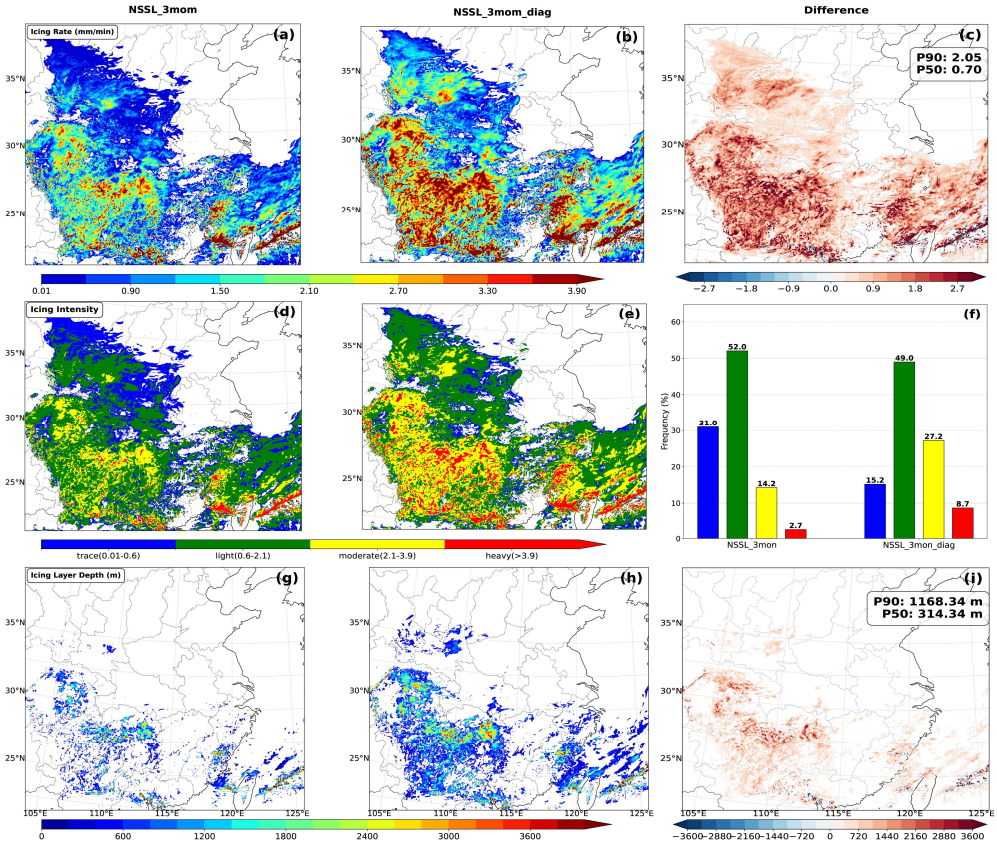


Figure 4. Aircraft icing rate (mm/min), intensity, and icing layer depth (m) at 0200 UTC on 9 March 2016 from simulations NSSL_3mon (a, d, g), and NSSL_3mom_diag (b, e, h), respectively. Note that the differences of the parameters between the two simulations are also shown in (c, f, i), with the 50th and 90th percentiles of the differences labeled in black on panels (c, i).